Research Article

A deep neural network potential model for transition metal diborides

Fu-Zhi Dai[1,2] (ID) **, Bo Wen[3,*], Yixuan Hu[4], Xin-Fu Gu[1,*]**

[1]School of Materials Science and Engineering, University of Science and Technology Beijing, Beijing 100083, China.
[2]AI for Science Institute, Beijing 100084, China.
[3]Science and Technology on Advanced Functional Composite Laboratory, Aerospace Research Institute of Materials and Processing Technology, Beijing 100076, China.
[4]School of Materials Science and Engineering, Shanghai Jiao Tong University, Shanghai 200240, China.

[*]**Correspondence to:** Dr. Bo Wen, Science and Technology on Advanced Functional Composite Laboratory, Aerospace Research Institute of Materials & Processing Technology, South Dahongmen Road 1#, Beijing 100076, China. E-mail: BHVeen@163.com; Prof. Xin-Fu Gu, School of Materials Science and Engineering, University of Science and Technology Beijing, Xueyuan Road 30#, Beijing 100083, China. E-mail: xinfugu@ustb.edu.cn

Abstract

Transition metal diborides (TMB_2s) are renowned for their high melting point and exceptional wear, corrosion, and erosion resistance, making them promising candidate materials for applications in extreme environments. As such, there is an urgent need for reliable material design tools for TMB_2s to improve efficiency in developing new materials. To address this need, we have developed a domain-specific medium-scale interatomic potential model for TMB_2s that encompasses elements Ti, Zr, Hf, V, Nb, Ta, Cr, Mo, W, and B. The prediction errors in energy and force of our model are 8.8 meV/atom and 387 meV/Å, respectively. Furthermore, the model demonstrates high accuracy in predicting various material properties, including lattice parameters, elastic constants, equations of states, and melting points, as well as grain boundary segregations. By providing a reliable and efficient tool for material design, this model will play a crucial role in the development of new, high-performance TMB_2s for use in extreme environments.

Keywords: Machine learning potential, atomic-scale simulation, transition metal diborides, melting point, grain boundary segregation

INTRODUCTION

Ultra-high temperature ceramics (UHTCs), encompassing transition metal diborides (TMB$_2$s), carbides, and nitrides, are renowned for their extraordinary properties such as high melting points, excellent wear, oxidation, and corrosion resistance, and exceptional strength[1-3]. These characteristics make UHTCs ideal candidate materials for applications in extreme environments, particularly within the aerospace, defense, and energy industries. Over the years, significant efforts have been made to improve the properties of UHTCs. These efforts include developing composite materials, employing micro-alloying techniques, and refining sintering methods[3-9]. Recently, the high entropy design paradigm has expanded from alloys to ceramics, leading to the development of numerous high-entropy UHTCs[10-16]. Regardless of whether micro-alloying is used in conventional UHTCs or heavy alloying in high-entropy UHTCs, there is an urgent need to understand: how elements are distributed within these materials; how alloying elements influence the microstructures and properties of the materials; and how we can tailor the alloying strategy based on the desired properties of the materials.

Atomic-scale simulations are powerful approaches in solving these problems, but they have long faced a dilemma between efficiency and accuracy. Density functional theory (DFT)-based methods offer high accuracy but suffer from extremely low efficiency. In contrast, molecular dynamics (MD) simulations based on classical interatomic potentials provide high efficiency but often with questionable accuracy. Fortunately, advancements in artificial intelligence have led to the development of machine learning potentials, which use machine learning models to learn from DFT datasets and generate interatomic potentials. Machine learning potentials bridge the gap between DFT and MD, ensuring that atomic-scale simulations maintain both high accuracy and high efficiency[17-22]. Several approaches have been employed to develop these potentials, including kernel ridge regression, Gaussian process regression, and artificial neural networks. These machine learning potentials have demonstrated significant promise in various applications in UHTCs, such as predicting material properties[23,24], investigating micro-mechanisms in materials[25,26], and aiding in materials design[5]. This breakthrough in materials research allows for more accurate and efficient atomic-scale simulations, opening new possibilities in the field.

In recent years, there has been significant progress in the development of machine learning potentials, particularly with the emergence of large models covering the entire periodic table. Numerous such models have been published in the past couple of years[20-22,27], demonstrating the potential of machine learning in understanding and predicting material properties. However, the training datasets for these models primarily consist of structures near equilibrium states, raising questions about their applicability to a diverse range of research fields. Furthermore, while these models are built on intricate neural network architectures to encompass the entire periodic table, their efficiency is greatly reduced, which limits their applicability for large-scale atomic simulations. To address these limitations, it is crucial to develop medium-scale models tailored for specific material types, which can serve as fundamental tools for materials simulation and design. In our study, we have focused on creating a medium-scale machine learning potential model for TMB$_2$s, encompassing elements Ti, Zr, Hf, V, Nb, Ta, Cr, Mo, W, and B. This model not only boasts accuracy comparable to DFT-based methods but also enables highly efficient atomic-scale simulations in diborides, including both conventional and high-entropy TMB$_2$s (HE-TMB$_2$s). We believe that this machine learning potential model holds great promise for the future of TMB$_2$s, paving the way for customizing and designing these materials to meet specific application requirements.

METHODS

Dataset collection

In this study, we adopt the machine learning potential model proposed by Zhang *et al.*, which is known as the Deep Potential (DP) model[17]. The DP model represents the potential energy surface using deep neural networks and consists of two sets of neural networks. The first set maps local atomic environments to symmetry-preserving descriptors, while the second set maps these descriptors to atomic energies[17]. We use the revised version of the DP model, called the DPA-1 model[28], which incorporates an element embedding mapping to improve generalizability and suitability for developing medium-scale interatomic potentials.

Training a machine learning potential requires a high-accuracy DFT dataset, containing atomic configurations and their corresponding energies, forces, and virial stresses. We collect the DFT dataset using the DP GENerator (DP-GEN) software, which generates the dataset under a concurrent learning scheme[29]. This scheme enriches the candidate DFT dataset iteratively in three steps: training, exploration, and labeling [Figure 1A]. Prior to the DP-GEN procedure, an initial dataset must be created. For this purpose, we produced 300 structures featuring random compositions and performed single-point first-principles calculations to generate the initial dataset. The approach for generating structures is consistent with the methodology employed in the second step of DP-GEN. The detailed DP-GEN processes are:

(1) During the training step, we train four DP models with different initialization parameters and activation functions based on existing data.

(2) In the exploration step, we explore the configurational space through MD simulations with DP models from the training step. We generate 100 diboride supercell structures with random compositions at the beginning of each iteration. A supercell with 72 atoms is created for each structure. The axes of the supercell are oriented along [420], [030], and [002] directions of TMB_2 (The crystal structure of TMB_2 is described in Supplementary Text 1 and illustrated in Supplementary Figure 1). Then, the metallic elements of the supercell are randomly occupied by the candidate elements. For example, the element is randomly generated from Ti, Zr, Hf, V, Nb, Ta, Cr, Mo, and W for each metallic site. Both bulk and surface structures are explored. For surface structures, the surface plane is randomly chosen from the x (normal to [420] direction), y (normal to [030] direction), and z (normal to [002] direction) planes of the supercell. For bulk structure sampling, we adopt the isothermal-isobaric (NPT) ensemble, with pressures ranging from 0 to 20 GPa (with a step of 5 GPa) and temperatures ranging from 300 to 6,000 K (with a step of 300 K). For surface structure sampling, we adopt the isothermal-isovolumic (NVT) ensemble, with temperatures ranging from 300 to 2,100 K.

(3) During the labeling step, we select candidate structures and label them using a DFT-based method. We randomly select the candidate structures from the MD trajectories based on "model deviation" (ε), which is the maximum standard deviation of forces predicted by the four DP models. We set two criteria for "model deviation": ε_{low} and ε_{high}. When $\varepsilon < \varepsilon_{low}$, all models predict similar values for the configuration, and adding the configuration to the dataset may only marginally improve the model. When $\varepsilon > \varepsilon_{high}$, the models have strong conflicts on the configuration, and there is a risk that the configuration is non-physical due to the inaccuracy of the current DP model. Adding the configuration to the dataset may disrupt the model. Therefore, we choose configurations with "model deviation" between ε_{low} and ε_{high} as candidates. The ε_{high} is set to be 2 eV/Å. The ε_{low} changes based on the exploration temperature (T), which are 0.3 eV/Å ($T < 2,000$ K), 0.5 eV/Å ($2,000$ K $< T < 4,000$ K), and 0.6 eV/Å ($4,000$ K $< T < 6,000$ K). We then label these candidate configurations using the Vienna ab initio simulation package (VASP)[30], adding them to the dataset. The calculations adopt the projector augmented wave (PAW)[31] approach to describe ion-electron interactions,
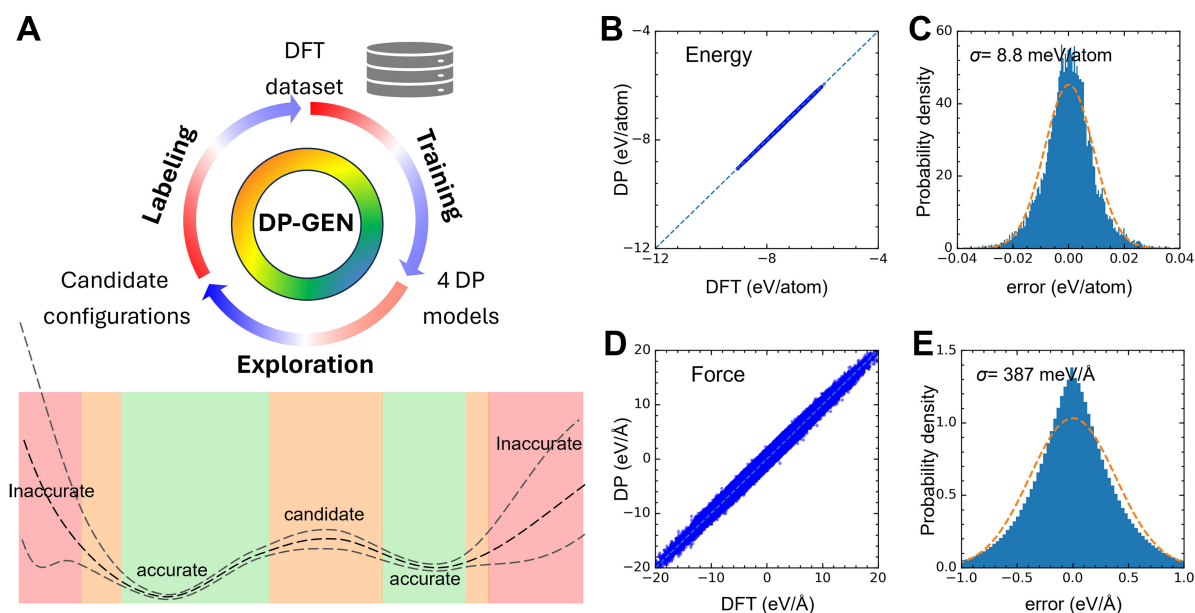
Figure 1. (A) Illustration of the DFT dataset generation process using a concurrent learning scheme in the DP-GEN software. The lower part of the image demonstrates the coverage of the configurational space by the current model, with accurate, candidate, and inaccurate regions distinguished by different colors; (B) Comparison of energy predictions between the DP model and DFT calculations; (C) Error distribution in predicted energy; (D) Comparison of force predictions between the DP model and DFT calculations; (E) Error distribution in predicted force. DFT: Density functional theory; DP-GEN: Deep Potential GENerator; DP: Deep Potential.

and the exchange-correction is described using the Perdew-Burke-Ernzerhof (PBE) generalized gradient approximation (GGA)[32]. We set the cutoff energy of the plane wave basis to 900 eV and adopt the Monkhorst-Pack[33] k-point mesh with a separation of 0.15 Å^{-1} in the Brillouin zone. Self-consistent field iteration stops when the difference in total energy of consecutive iterations is less than 10^{-6} eV.

Model training
After collecting the dataset, the DP model was trained using the DeePMD-kit software[34,35], specifically employing the DPA-1 model. The architecture of the DP model was established as follows:

(1) The descriptor net maps atomic environments to symmetry-preserving descriptors, utilizing a network type set as "se_atten_v2". The "se_atten_v2" type in DeePMD-kit software designation refers to the DPA-1 model architecture, as detailed in the reference[28]. The element embedding net consists of a single-layer neural network with eight nodes. The descriptor net is composed of three layers of neural networks, each containing 25, 50, and 100 nodes, respectively. The projection dimension is set to 16, and the cutoff is set to 7.0 Å with a smooth function imposed from 6.0 Å. The activation functions used are tanh.

(2) The fitting net maps the descriptors to atomic energies, including three layers of neural networks with each having 128 nodes. A ResNet (residual network) architecture is adopted in the fitting net, and the activation functions are also tanh.

The model was trained in two steps with the "Adam" optimizer. During the first step, the learning rate, which scales the loss that feeds to the optimizer, decayed from 1.0×10^{-3} to 1.0×10^{-8}, and the pre-factors of energy, force, and virial in the loss function changed from 0.1 to 1, from 100 to 1, and from 0.1 to 1, respectively. Subsequently, the model was retrained, inheriting the model parameters from the first training

round. In this round, the learning rate decayed from 1.0×10^{-4} to 1.0×10^{-8}, and the pre-factors of energy, force, and virial in the loss function were set to 10, 1, and 1, respectively, remaining constant. In each training round, the total training step amounted to 8 million. For further details regarding the parameters, one may refer to ref[34,35] and the open-source software. The DeePMD method has been successfully integrated into the open-source MD simulation software LAMMPS[36]. Subsequent simulations were performed using LAMMPS with the trained DP model.

RESULTS AND DISCUSSION

The accuracy of the DP model was first examined by comparing its predictions to DFT calculations. Figure 1B compares the energy prediction by the DP model and the DFT calculations, while Figure 1C presents the distribution of the prediction error in energy values. Similarly, Figure 1D displays the comparison between the forces predicted by the DP model and the DFT calculations, and Figure 1E highlights the error distribution concerning the prediction error in the force values. The results demonstrate a high level of agreement between the DP model and the DFT calculations. The prediction errors in energy and force values stand at 8.8 meV/atom and 387 meV/Å, respectively. It is important to note that these prediction errors are in line with those observed in numerous other comparable systems, as documented in ref[5,23-26]. In the subsequent analysis, the DP model will be utilized to compute fundamental properties, predict melting points, and simulate grain boundary segregations. This will demonstrate the model's capabilities and effectiveness.

Prediction on fundamental properties

In addition to the comparable predictions of energy and force between the DP model and DFT calculations, it is crucial to assess the reliability of the DP model in predicting material properties. Table 1 presents a comparison of the lattice parameters (*a* and *c*), cohesive energy (*E*), and elastic constants (C_{11}, C_{12}, C_{13}, C_{33}, and C_{44}) of TMB_2s (TM = Ti, Zr, Hf, V, Nb, Ta, Cr, Mo, W) as predicted by the DP model and the DFT calculations, where a good agreement can be observed. Although the model demonstrates high accuracy, it inadequately fits certain properties, such as WB_2's C_{33} depicted in Table 1. Fitting properties of unstable materials typically poses a greater challenge. The stability of TMB_2s was assessed by examining their phonon dispersion curves [Supplementary Figure 2], where imaginary modes were detected for CrB_2, MoB_2, and WB_2. The equation of state characterizes the variation of energy with respect to volume changes, which can be determined by relaxing the structures at different volumes. Figure 2 displays a comparison of the equations of state for TMB_2 (TM = Ti, Zr, Hf, V, Nb, Ta, Cr, Mo, W) as predicted by the DP model and the DFT calculations, all of which exhibit good agreements.

Melting point prediction

The family of TMB_2s is well-known for their high melting points, with some exhibiting melting points higher than 3,000 °C and being classified as UHTCs[2]. Solid solutions are crucial for tailoring the properties of TMB_2s, such as removing harmful impurities, enhancing sintering, and improving high-temperature strength[4,6,37]. In recent years, the high-entropy concept was introduced to ceramics, leading to the synthesis of new high-entropy diborides[11,13]. HE-TMB_2s are believed to possess high melting points, high hardness, and other properties, making them promising candidate materials for extreme environments. However, the melting points of these high-entropy diborides are unknown, and the effects of solid solutions on their melting points are unclear.

In this section, the DP model is used to predict the melting points of diborides and to investigate the effects of solid solutions on melting points. TMB_2s (TM = Ti, Zr, Hf, V, Nb, Ta, Cr, Mo, W) were simulated, along with high-entropy compounds $Zr_{0.25}Hf_{0.25}Nb_{0.25}Ta_{0.25}B_2$ (HEMB$_2$_4), $Ti_{0.2}Zr_{0.2}Hf_{0.2}Nb_{0.2}Ta_{0.2}B_2$ (HEMB$_2$_Ti),

Table 1. Comparison of lattice parameters (*a* and *c*), cohesive energy (*E*), and elastic constants (C_{11}, C_{12}, C_{13}, C_{33}, and C_{44}) of TMB$_2$ (TM = Ti, Zr, Hf, V, Nb, Ta, Cr, Mo, W) predicted by the DP model and DFT calculations

		a (Å)	*c* (Å)	*E* (eV/atom)	C_{11} (GPa)	C_{12} (GPa)	C_{13} (GPa)	C_{33} (GPa)	C_{44} (GPa)
TiB$_2$	DFT	3.033	3.226	-8.144	650	65	105	445	258
	DP	3.038	3.214	-8.139	650	98	91	426	248
ZrB$_2$	DFT	3.172	3.543	-8.327	563	56	119	434	249
	DP	3.176	3.541	-8.319	566	86	141	369	261
HfB$_2$	DFT	3.143	3.487	-8.801	599	69	122	458	264
	DP	3.151	3.469	-8.793	583	83	150	468	283
VB$_2$	DFT	2.998	3.026	-8.211	684	119	122	490	227
	DP	3.001	3.037	-8.208	628	132	143	407	227
NbB$_2$	DFT	3.109	3.323	-8.610	603	112	183	439	223
	DP	3.110	3.328	-8.613	560	110	174	447	206
TaB$_2$	DFT	3.103	3.324	-9.054	605	138	199	455	212
	DP	3.104	3.330	-9.056	601	167	209	442	186
CrB$_2$	DFT	2.977	2.935	-7.973	592	175	200	352	166
	DP	2.978	2.928	-7.970	668	197	147	345	212
MoB$_2$	DFT	3.029	3.331	-8.407	595	133	223	398	149
	DP	3.034	3.324	-8.407	584	143	241	323	105
WB$_2$	DFT	3.020	3.373	-8.866	619	153	243	414	136
	DP	3.007	3.420	-8.861	643	181	267	287	57

TMB$_2$: Transition metal diboride; DP: Deep Potential; DFT: density functional theory.
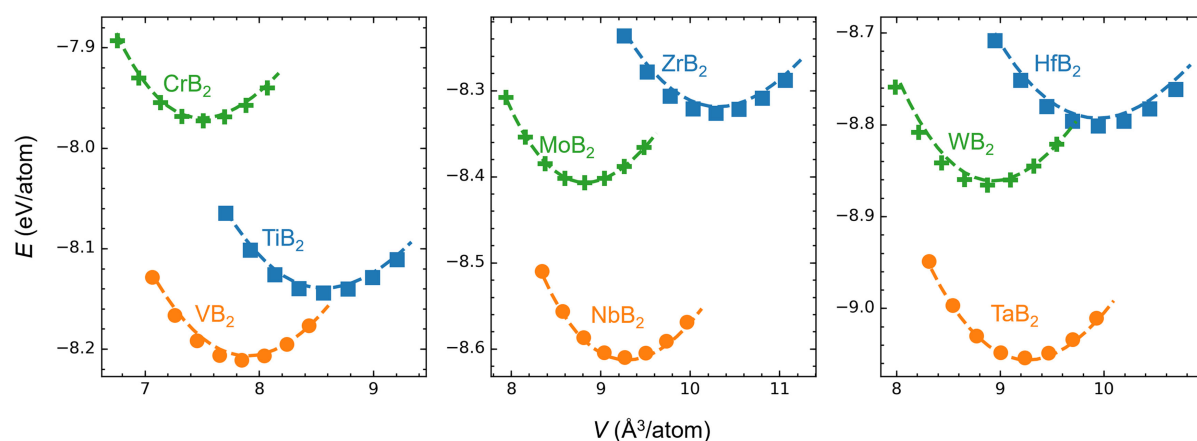

Figure 2. Comparison of equations of state of TMB$_2$ (TM = Ti, Zr, Hf, V, Nb, Ta, Cr, Mo, W) predicted by the DP model (dash line) with the DFT calculations (points). TMB$_2$: Transition metal diboride; DP: Deep Potential; DFT: density functional theory.

V$_{0.2}$Zr$_{0.2}$Hf$_{0.2}$Nb$_{0.2}$Ta$_{0.2}$B$_2$ (HEMB$_2$_V), and W$_{0.2}$Zr$_{0.2}$Hf$_{0.2}$Nb$_{0.2}$Ta$_{0.2}$B$_2$ (HEMB$_2$_W). The solid-liquid coexistence method was employed to simulate the melting points of these compounds. The simulation box was aligned along the [010], [001], and [210] directions, with lengths of 8 × 8 × 10 (X × Y × Z) along each direction. The solid-liquid interfaces were parallel to the XY plane. The solid, solid-liquid coexistence, and liquid states are illustrated in Figure 3A.

During MD simulations, the timestep was set to 1 fs, and the NPT ensemble was adopted with *P* = 0 Pa and pressure control applied independently in each direction. The damping parameters were set to 500 fs for
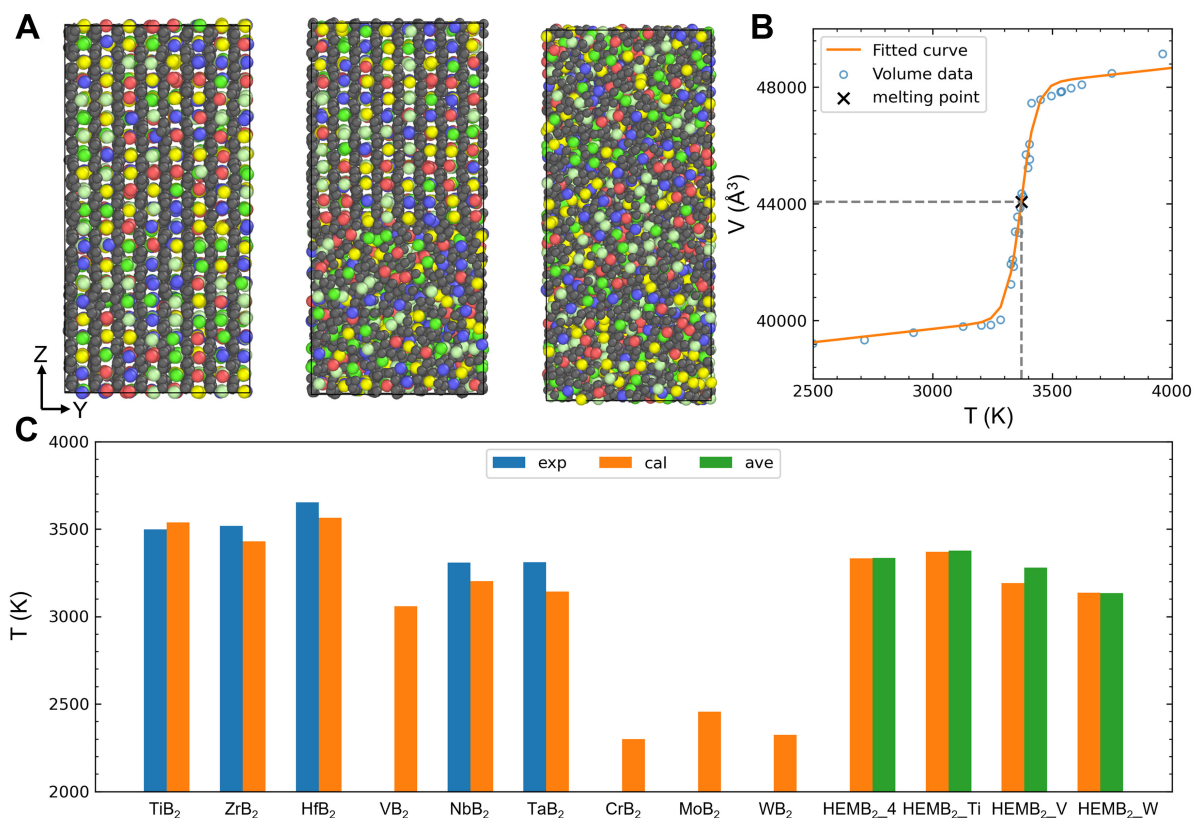
Figure 3. (A) The snapshots of solid, solid-liquid coexistence, and liquid states of HEMB$_2$_Ti during MD simulations; (B) Illustration of how the melting point value is determined based on V~T data; (C) Comparison of experimentally measured and calculated melting points of TMB$_2$s, as well as the calculated melting points of HE-TMB$_2$s, and the estimated values obtained by averaging the melting points of their constituent compounds. The composition of HEMB$_2$_4, HEMB$_2$_Ti, HEMB$_2$_V and HEMB$_2$_W are Zr$_{0.25}$Hf$_{0.25}$Nb$_{0.25}$Ta$_{0.25}$B$_2$, Ti$_{0.2}$Zr$_{0.2}$Hf$_{0.2}$Nb$_{0.2}$Ta$_{0.2}$B$_2$, V$_{0.2}$Zr$_{0.2}$Hf$_{0.2}$Nb$_{0.2}$Ta$_{0.2}$B$_2$, and W$_{0.2}$Zr$_{0.2}$Hf$_{0.2}$Nb$_{0.2}$Ta$_{0.2}$B$_2$, respectively. Melting point values are listed in Supplementary Table 1. MD: Molecular dynamics; HE-TMB$_2$s: high-entropy transition metal diborides.

pressure and 100 fs for temperature. The system was first equilibrated at a solid temperature (T_{solid}) close to the melting point for 50 ps. Then, half of the system was heated to a high temperature (T_{liquid}) and melted, while the other half remained frozen for 50 ps. This process resulted in a solid-liquid coexistence state. Finally, the entire system was set to another temperature (T) and equilibrated for 1 ns. T_{solid} and T_{liquid} were fixed for each compound, and the system with a series of T values was analyzed. For different Ts, the final state could be solid, solid-liquid coexistent, or liquid [Figure 3A]. The volume (V) *vs.* T data was collected from the simulations and fitted with a sigmoid-like function:

$$V = \frac{b}{1 + \exp(-a(T - T_0))} + cT + V_0$$

where a, b, c, T_0, and V_0 are fitting parameters. The linear expansion effect is accounted for by $cT + V_0$, while the sigmoid function $\frac{b}{1+\exp(-a(T-T_0))}$ represents the volume jump during melting, and T_0 is the melting point. Figure 3B shows the V~T data of HEMB$_2$_Ti and how well the equation fits the data. The midpoint of the jump is defined as the melting point.

Figure 3C displays the predicted melting points for all mono-compounds, experimentally measured data for TiB$_2$, ZrB$_2$, HfB$_2$, NbB$_2$, and TaB$_2$ by Ruby *et al.*, and estimated melting points for HEMB$_2$s by averaging the melting points of their constituent compounds[38]. The results demonstrate that the melting points predicted by our DP model closely match experimental measurements, indicating the model's accuracy. For high-entropy compounds, their melting points closely align with the average values of their constituent compounds. This finding suggests that the mean value is a suitable initial estimate for the melting point of HE-TMB$_2$s. The melting points of unstable compounds MoB$_2$ and WB$_2$ are also plotted in Figure 3C, which cannot be measured experimentally. With these values for mono-compounds and the mean value approach, the melting point of any composition can be estimated, which can be applied in the future for a better design of high-entropy diborides.

Grain boundary segregation

Grain boundary engineering through solid solution segregation has emerged as a promising strategy to improve the high-temperature strength of diboride and carbide UHTCs. This approach has been validated by both experimental evidence[6,37,39-41] and theoretical simulations[25,26], and has proven effective for both conventional and high-entropy UHTCs[40,41].

In this section, we demonstrate the capabilities of the DP model in simulating grain boundary segregation and its enhancement of grain boundaries. We constructed 14 symmetric tilt grain boundaries, similar to our previous work[26]. The construction method is detailed in Supplementary Text 2, Supplementary Figure 3 and Supplementary Table 2. A grain boundary plane can be defined by two in-plane vectors, which are contained in its name. One is the rotation axis of the tilt grain boundary. The other is a combination of the other two basis vectors. For example, the 010_21 grain boundary has a rotation axis of [010] and another in-plane direction of 2[001]+[$\overline{2}$10], while the 210_12 grain boundary has a rotation axis of [210] and another in-plane direction of [001]+2[010]. For more information of the constructed grain boundaries [Supplementary Table 2]. The relaxed atomic structure of each grain boundary in ZrB$_2$ is shown in Supplementary Figure 4. Hybrid Monte Carlo/molecular dynamics (MC/MD) simulations were employed to examine grain boundary segregations. The simulations were performed under the NPT ensemble with P = 0 Pa, T = 2,000 K, and a time step of 1 fs. The damping parameters were set to 500 fs for pressure and 100 fs for temperature. Any pair of different metallic elements was swapped every five MD steps, with the acceptance probability of swapping following the Metropolis criterion: min(1, exp(-$\Delta E/k_B T$)), where ΔE is the energy change due to swapping and k_B is Boltzmann's constant. The total MC/MD simulation duration was 500,000 steps. A virtual tensile simulation was adopted to evaluate grain boundary strength, aligning the tensile direction normal to the grain boundary plane. The last snapshot of the MC/MD simulation was used to calculate grain boundary strength. The tensile simulations were conducted under the NPT ensemble at 2,000 K and an in-plane pressure of 0 Pa, with no constraints on stress along the tensile direction. The time step and damping parameters were consistent with those used in the segregation simulations, and the strain rate was set to 1×10^9 s^{-1}. During tensile simulation, stress variation is approximately 1 GPa in the tensile direction. Consequently, when the strength difference is less than 1 GPa, distinguishing which grain boundary is stronger becomes inconclusive due to the margin of error.

Initially, we investigated W segregation in ZrB$_2$ grain boundaries and the grain boundary strengthening effect it caused. The average W concentration at the metallic sites is established at 5 at%, marginally exceeding the experimentally determined W levels in ZrB$_2$ bulk, which range between 2 at% and 4 at%[8]. Following MC/MD simulations, W content in the bulk decreases owing to grain boundary segregation, aligning the concentration with experimental observations. Figure 4A displays the occupation probability of W at each metallic site for the 010_21 and 210_11 grain boundaries. Snapshots were extracted every 1,000 steps from steps 250,000 to 500,000 for statistical analysis. The occupation probability of a given site was
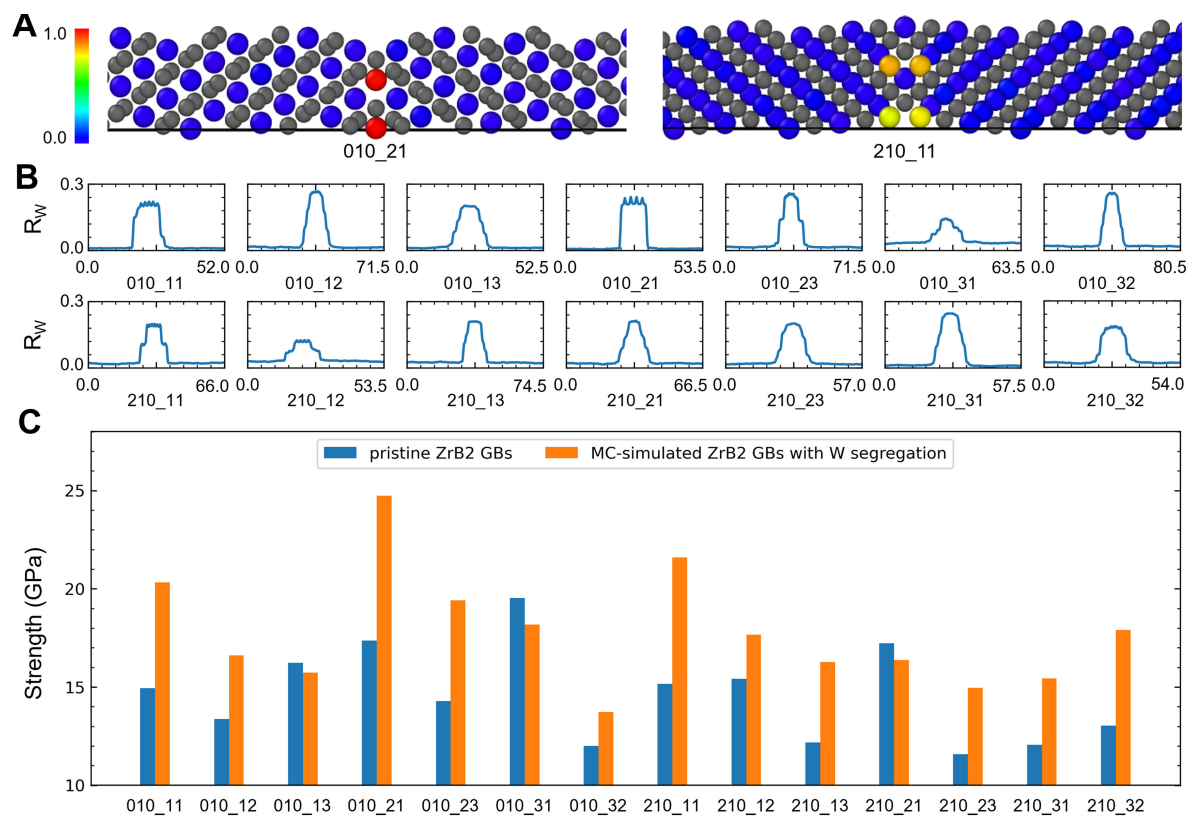
Figure 4. (A) The occupation probability of W at each metallic site, with noticeable W segregation around grain boundaries. W forms a monolayer at the grain boundary plane in the 010_21 grain boundary, while it forms an off-center bilayer pattern in the 210_11 grain boundary. Gray atoms are B, and colored atoms are metals; (B) The concentration profile of W (R_W) at the metallic site surrounding various grain boundaries, displaying prominent W segregation around these boundaries. The unit of horizontal axis is Å; (C) A comparison of the ideal grain boundary strength between pure ZrB_2 and ZrB_2 with W segregation. Ideal grain boundary strength values are listed in Supplementary Table 3.

calculated by N_W/N_{frames}, where N_{frames} is the total number of selected frames and N_W accounts for the number of times the site is occupied by W. Noticeable W segregation around grain boundaries can be observed in Figure 4A, with W forming a monolayer at the grain boundary plane in the 010_21 grain boundary and an off-center bilayer pattern in the 210_11 grain boundary. In our earlier studies[26,42], we demonstrated that size effects predominantly govern segregation behavior, leading to W atoms favoring smaller-sized grain boundary sites. The segregation pattern is mainly governed by the strain state of each grain boundary[26]. Additionally, the concentration profiles of W (R_W) were calculated from the selected frames. Slices parallel to the grain boundary plane with a thickness of 10 Å were cut, and the W concentration in the slice was adopted as the concentration at the midpoint of the slice. Figure 4B displays the W concentration profiles of all calculated grain boundaries, revealing prominent W segregation around these boundaries, with W concentrations around grain boundaries reaching as high as ~20 at% in metallic sites, which are much higher than W contents in the bulk. Figure 4C compares the ideal grain boundary strength between pure ZrB_2 and ZrB_2 with W segregation. For pristine ZrB_2 grain boundaries, the strength of the grain boundaries investigated in this study mainly depends on two factors. First, grain boundaries such as the 010_32, 210_13, and 210_23 types demonstrate low strength attributed to improperly self-accommodated structures, as evidenced by the strained B–B bonds near the grain boundaries. The relaxed structures in Supplementary Figure 4 show some bonds extending over 2 Å, signaling the weak bonding character of these grain boundaries and hence their reduced strength; Second, the strength of well-self-accommodated grain

boundaries is influenced by their orientation relative to the boron net plane. Typically, a smaller angle between the grain boundary normal and the boron net plane correlates with higher strength, as exemplified by the robust 010_31 grain boundary. With W segregation, the results indicate that most of the grain boundaries are significantly enhanced (improved by ~30%), except 010_13, 010_31, and 210_21, where the ideal strengths decrease slightly within the error level of calculation. Due to the large size of Zr, some of the boron bonds around grain boundaries are stretched and weakened, leading to low strength. Replacing Zr by W around grain boundaries is equivalent to introducing additional compressive strains to grain boundaries, reducing boron bond lengths around grain boundaries, which then enhances grain boundaries[26]. Especially for the 010_21 boundary, segregation of W will increase its strength substantially, which fractures shifting by one atomic layer into one of the crystals instead of the grain boundary plane[26]. The enhancement induced by segregation is highly dependent on the atomic structure of a grain boundary. For instance, the 010_21 grain boundary exhibits the smallest in-plane periodicity [Figure 4A and Supplementary Figure 4], which allows near-total coverage by segregated W atoms at the boundary sites. This near total occupancy, if it indeed reinforces local strength, would result in considerable strengthening of the entire boundary. Conversely, a larger in-plane periodicity, as in the 010_13 grain boundary, results in tungsten atoms replacing only some sites[26], leading to a lower degree of segregated coverage. Subsequently, the strength of this grain boundary is marginally influenced by segregation. The reduction in the ideal strength of the 010_31 boundary is consistent with our previous findings[26], where the W segregation level in this boundary is minimal [Figure 4B]. After MC/MD simulation, we obtained an asymmetrical segregation pattern of W around the boundary. Such asymmetry destroys the well-accommodated structure, potentially weakening the grain boundary. For the 210_21 grain boundary, additional space permits increased W segregation. As indicated in Supplementary Figure 4, the metal elements shift to one side of the grain boundary in the 210_21 boundary, creating a large volume on the opposite side. The MC/MD methods employed here are incapable of filling this free volume, likely contributing to the slightly diminished grain boundary strength. Nevertheless, most of the grain boundaries can be enhanced due to grain boundary segregation, which may improve high temperature strength of ZrB_2, agreeing with experimental observations[6,37,39].

In addition to micro-alloying for creating conventional solid solutions, heavily alloying with multiple elements to produce medium- or high-entropy diborides is another effective method for tailoring material properties. Our previous work has reported grain boundary segregation in medium- and high-entropy carbides through simulations, as well as the grain boundary strengthening effect due to segregation[25]. Here, the DP model is employed to investigate grain boundary segregation in a medium-entropy diboride $Ti_{1/3}Zr_{1/3}Hf_{1/3}B_2$ (ME-TMB$_2$). Figure 5A illustrates the occupation probability of Ti at each metallic site in the 010_21 and 210_11 grain boundaries, with results similar to W segregation in ZrB_2 grain boundaries. Ti forms a monolayer at the grain boundary plane in the 010_21 grain boundary, and adopts an off-center bilayer pattern in the 210_11 grain boundary with Ti depletion at the grain boundary plane. Figure 5B presents the concentration profile of Ti (R_{Ti}) at the metallic site surrounding various grain boundaries, indicating significant Ti segregation around most of these boundaries. The concentration increase of Ti is not as substantial as W in ZrB_2 grain boundaries, suggesting a lower segregation tendency of Ti. Figure 5C compares the grain boundary strength of pure ZrB_2 and $Ti_{1/3}Zr_{1/3}Hf_{1/3}B_2$ after MC/MD simulations, demonstrating that all the grain boundaries of $Ti_{1/3}Zr_{1/3}Hf_{1/3}B_2$ are stronger. This finding indicates that medium- or high-entropy approaches are also effective in designing diborides with robust high-temperature strength.

To further enhance grain boundaries and improve high-temperature strength, we can incorporate micro-alloying into medium- or high-entropy diborides, such as by introducing a solid solution of W into $Ti_{1/3}Zr_{1/3}Hf_{1/3}B_2$. We added 5 at% of W to the metallic site of $Ti_{1/3}Zr_{1/3}Hf_{1/3}B_2$ and then simulated segregation.
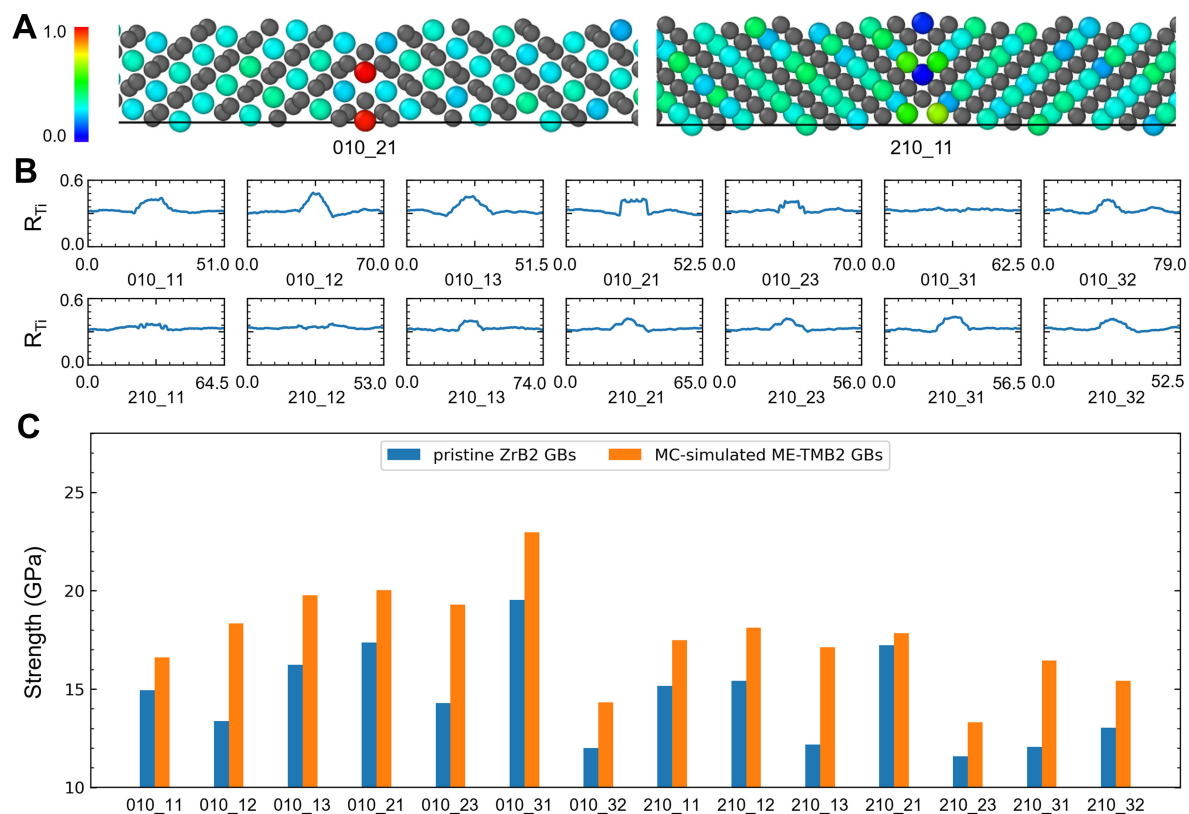
Figure 5. (A) The occupation probability of Ti at each metallic site, with noticeable Ti segregation around grain boundaries. Ti forms a monolayer at the grain boundary plane in the 010_21 grain boundary, while it forms an off-center bilayer pattern in the 210_11 grain boundary. Gray atoms are B, and colored atoms are metals; (B) The concentration profile of Ti (R_{Ti}) at the metallic site surrounding various grain boundaries, displaying prominent Ti segregation around most of these boundaries. The unit of the horizontal axis is Å; (C) A comparison of the ideal grain boundary strength between pure ZrB_2 and medium-entropy $Ti_{1/3}Zr_{1/3}Hf_{1/3}B_2$ (ME-TMB$_2$) after MC/MD simulation. Ideal grain boundary strength values are listed in Supplementary Table 3. MC/MD: Hybrid Monte Carlo/molecular dynamics.

As illustrated in Figure 6A, substantial W segregations were obtained, similar to those in ZrB_2, with Ti depletion occurring around grain boundaries due to W's higher segregation tendency. Figure 6B displays a comparison of the grain boundary strengths between $Ti_{1/3}Zr_{1/3}Hf_{1/3}B_2$ alloys with and without W segregation. It highlights that the grain boundaries 010_11, 010_21, 210_11, 210_23, and 210_32 experience a significant reinforcement from W micro-alloying. All of these grain boundaries have normals that form a small angle with the boron net plane. While certain other grain boundaries display slight improvements or weakenings owing to W micro-alloying, these changes fall within the limits of calculation error. In general, the findings demonstrate that, on average, W segregation contributes to the enhancement of grain boundary strengths. This result indicates that combining the medium/high-entropy design strategy with the micro-alloy strategy is effective in designing new high-performance materials.

When generating the training data for the DP model, no grain boundary structure is included. We examine the reliability of the DP model in predicting grain boundaries by evaluating grain boundary energies and segregation energies, with the results shown in Supplementary Text 3, Supplementary Table 4 and Supplementary Figure 5. Even though the DP model does not exhibit the same high accuracy as it does for other properties, its predictive capabilities on grain boundaries are reasonable, correctly capturing the elementary dependent grain boundary properties. In addition, our simulation results are in good agreement
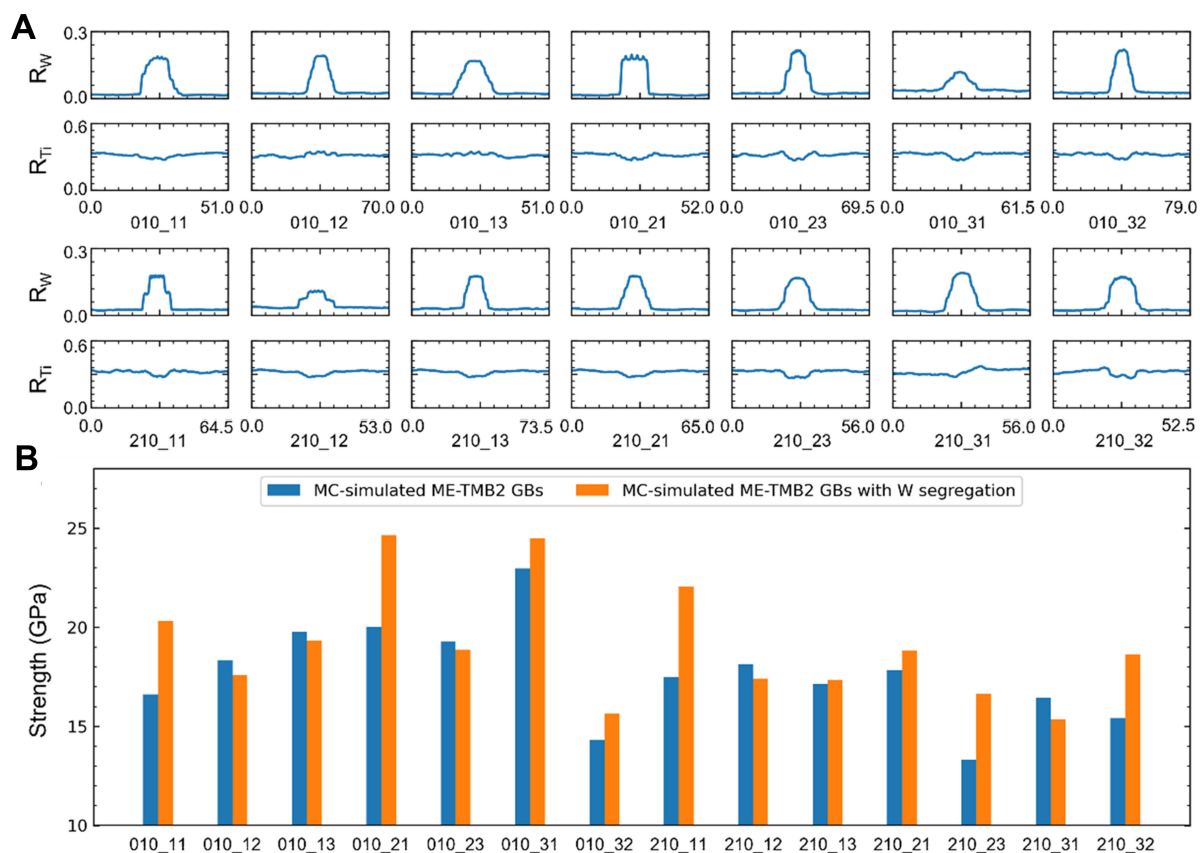
Figure 6. (A) The concentration profile of W (R_W) and Ti (R_{Ti}) at the metallic site surrounding various grain boundaries, displaying prominent W segregation around these boundaries, which results in Ti depletion around these boundaries. The unit of the horizontal axis is Å; (B) A comparison of the ideal grain boundary strength between pure $Ti_{1/3}Zr_{1/3}Hf_{1/3}B_2$ (ME-TMB$_2$) and $Ti_{1/3}Zr_{1/3}Hf_{1/3}B_2$ with W segregation. Ideal grain boundary strength values are listed in Supplementary Table 3.

with previous simulations on ZrB_2 with a solid solution of W[26], and they also correspond well with experimental results in ZrB_2 and $Ti_{1/3}Zr_{1/3}Hf_{1/3}B_2$[4,6,11,37,43]. In experiments, the segregation of W into ZrB_2 grain boundaries has been confirmed by transmission electron microscopy[39]. Furthermore, the high-temperature fracture surface transforms from being dominated by intergranular features to being dominated by transgranular features with the addition of WC[6]. The grain boundaries also exhibit improved thermal corrosion resistance[37], which indicates a reduction in grain boundary energy and an enhancement in grain boundary strength due to W segregation. As reported in ref[11], similar to ZrB_2 with WC as a sintering additive, medium-entropy $Ti_{1/3}Zr_{1/3}Hf_{1/3}B_2$ also demonstrates good strength retention at elevated temperatures, and the addition of WC can further improve the strength of $Ti_{1/3}Zr_{1/3}Hf_{1/3}B_2$, which is consistent with our simulation results. In addition to the strengthening effect, the addition of WC can also help remove surface oxides, resulting in cleaner grain boundaries[4]; pin grain boundaries, leading to an improved microstructure uniformity; and increase grain boundary oxidation resistance due to the low activation of W.

Discussion

In previous sections, we have demonstrated the accuracy and reliability of the DP model in predicting various properties, such as lattice parameters, elastic constants, equations of state, melting points, and grain boundary segregations. This indicates that our DP model can be effectively applied to TMB$_2$ mono-compounds or solid solutions, regardless of whether they are micro-alloyed, heavily alloyed, or even

designed as high-entropy materials. Consequently, the model serves as an efficient and accurate tool for predicting material properties, exploring micro-mechanisms, and ultimately assisting in material design. This paves the way for the customization and design of these materials to meet the demands of various applications.

While the model shows good accuracy, a few properties have not been well fitted, such as the C_{33} of WB_2, as shown in Table 1. In machine learning potentials, there is still a need to strike a balance between accuracy and efficiency. The DPA-1 model achieves a satisfactory balance between these two factors, making it a suitable choice for simulating systems with up to 10,000 atoms. The prediction errors in energy and force values for this model are 8.8 meV/atom and 387 meV/Å, respectively. If a more accurate model is required, one can opt for a more complex model, such as the DPA-2 model[27] available in the DeePMD-kit software. This model can improve the prediction error by approximately 30%, with errors in energy and force being 6.0 meV/atom and 245 meV/Å, respectively. However, this increased accuracy comes at the cost of reduced efficiency, which is one to two orders of magnitude slower than the DPA-1 model. As a result, the DPA-2 model may only be suitable for simulations involving hundreds to thousands of atoms. For scenarios where simulations with millions of atoms are frequently conducted, a more efficient model is needed, such as the NVNMD model[44] in the DeePMD-kit software. This model offers an efficiency that is one order of magnitude faster than the DPA-1 model. However, the trade-off is an increase in prediction errors for energy and force values, which rise to 13.2 meV/atom and 410 meV/Å, respectively.

In addition to the models, our highly precise DFT dataset also plays a significant role in the impending revolution of atomic-scale simulations. The potential of big machine learning models is set to bring about substantial changes to the field of material research. In order to develop reliable big machine learning potential models, it is crucial not only to create new artificial intelligence models but also to enrich valuable datasets for model training. While large high-throughput DFT datasets have already been developed under the support of the Materials Genome Initiative, such as the Materials Project[45], AFLOW[46], and OQMD[47], there is still a need for many domain-specific datasets to cater to the varying demands of different fields. These datasets will not only aid in the development of big machine learning potential models but also assist in driving the revolution in materials research. By focusing on enriching our dataset resources and refining our artificial intelligent models, we can truly unlock the full potential of atomic-scale simulations and revolutionize the field of material research.

CONCLUSIONS

In this study, we have developed a medium-scale interatomic potential model for TMB_2s, which is based on the DPA-1 machine learning potential model. This model encompasses elements Ti, Zr, Hf, V, Nb, Ta, Cr, Mo, W, and B, making it suitable for simulating TMB_2 mono-compounds or solid solutions.

The prediction errors of our model are 8.8 meV/atom for energy and 387 meV/Å for force, respectively. Moreover, the model demonstrates high accuracy in predicting various material properties, including lattice parameters, elastic constants, and melting points. Additionally, we have showcased the model's ability to simulate grain boundary segregation in TMB_2s, where our simulations exhibit excellent agreement with experimental measurements.

This domain-specific medium-scale model enables researchers to predict material properties, investigate micro-mechanisms in TMB_2s, and facilitate materials design based on specific requirements. We believe that the machine learning potential model developed in this work holds significant promise for the future of TMB_2s research, paving the way for the customization and design of these materials to meet the demands of various applications.

DECLARATIONS

Note

Declaration of generative AI and AI-assisted technologies in the writing process: during the preparation of this work, the author(s) used ChatGPT in order to improve language and readability. After using this tool/service, the author(s) reviewed and edited the content as needed and take(s) full responsibility for the content of the publication.

Authors' contributions

Investigation, methodology, validation, visualization, writing, review and editing: Dai FZ
Funding acquisition, validation, review and editing: Wen B
Validation, visualization, writing - review and editing: Hu Y
Project administration, supervision, writing, review and editing: Gu XF

Availability of data and materials

The DFT dataset and the DP model have been uploaded to the website (https://www.aissquare.com/) for free download.

Conflicts of interest

Dai FZ is the guest editor of the special issue, while the other authors have declared that they have no conflicts of interest.

Ethical approval and consent to participate

Not applicable.

Consent for publication

Not applicable.

Copyright

REFERENCES

1. Opeka MM, Talmy IG, Zaykoski JA. Oxidation-based materials selection for 2000 °C + hypersonic aerosurfaces: theoretical considerations and historical experience. *J Mater Sci* 2004;39:5887-904. DOI
2. Fahrenholtz WG, Hilmas GE, Talmy IG, Zaykoski JA. Refractory diborides of zirconium and hafnium. *J Am Ceram Soc* 2007;90:1347-64. DOI
3. Ni D, Cheng Y, Zhang J, et al. Advances in ultra-high temperature ceramics, composites, and coatings. *J Adv Ceram* 2022;11:1-56. DOI
4. Zou J, Zhang GJ, Hu CF, et al. Strong ZrB$_2$-SiC-WC ceramics at 1600 °C. *J Am Ceram Soc* 2012;95:874-8. DOI
5. Wang Y, Wen B, Jiao X, et al. The highest melting point material: searched by Bayesian global optimization with deep potential molecular dynamics. *J Adv Ceram* 2023;12:803-14. DOI
6. Ma HB, Man ZY, Liu JX, Xu FF, Zhang GJ. Microstructures, solid solution formation and high-temperature mechanical properties of

ZrB_2 ceramics doped with 5vol.% WC. *Mater Design* 2015;81:133-40. DOI

7. Silvestroni L, Gilli N, Migliori A, et al. A simple route to fabricate strong boride hierarchical composites for use at ultra-high temperature. *Compos Part B Eng* 2020;183:107618. DOI

8. Silvestroni L, Failla S, Vinokurov V, Neshpor I, Grigoriev O. Core-shell structure: an effective feature for strengthening ZrB_2 ceramics. *Scr Mater* 2019;160:1-4. DOI

9. Silvestroni L, Mungiguerra S, Sciti D, Di Martino GD, Savino R. Effect of hypersonic flow chemical composition on the oxidation behavior of a super-strong UHTC. *Corros Sci* 2019;159:108125. DOI

10. Chen H, Xiang H, Dai FZ, Liu J, Zhou Y. Porous high entropy $(Zr_{0.2}Hf_{0.2}Ti_{0.2}Nb_{0.2}Ta_{0.2})B_2$: a novel strategy towards making ultrahigh temperature ceramics thermal insulating. *J Mater Sci Technol* 2019;35:2404-8. DOI

11. Li RZ, Wang XG, Yuan JH, et al. Enhanced high-temperature strength in textured $(Ti_{1/3}Zr_{1/3}Hf_{1/3})B_2$ medium-entropy ceramics via strong magnetic field. *J Am Ceram Soc* 2023;106:5440-53. DOI

12. Yang QQ, Wang XG, Wu P, et al. Ultra-high strength medium-entropy (Ti,Zr,Ta)C ceramics at 1800 °C by consolidating a core-shell structured powder. *J Am Ceram Soc* 2022;105:823-9. DOI

13. Feng L, Chen WT, Fahrenholtz WG, Hilmas GE. Strength of single-phase high-entropy carbide ceramics up to 2300 °C. *J Am Ceram Soc* 2021;104:419-27. DOI

14. Gild J, Zhang Y, Harrington T, et al. High-entropy metal diborides: a new class of high-entropy materials and a new type of ultrahigh temperature ceramics. *Sci Rep* 2016;6:37946. DOI PubMed PMC

15. Xiang H, Xing Y, Dai F, et al. High-entropy ceramics: present status, challenges, and a look forward. *J Adv Ceram* 2021;10:385-441. DOI

16. Wen Z, Tang Z, Liu Y, Zhuang L, Yu H, Chu Y. Ultrastrong and high thermal insulating porous high-entropy ceramics up to 2000 °C. *Adv Mater* 2024;36:e2311870. DOI PubMed

17. Zhang L, Han J, Wang H, Car R, Weinan E. Deep potential molecular dynamics: a scalable model with the accuracy of quantum mechanics. *Phys Rev Lett* 2018;120:143001. DOI

18. Behler J, Parrinello M. Generalized neural-network representation of high-dimensional potential-energy surfaces. *Phys Rev Lett* 2007;98:146401. DOI PubMed

19. Bartók AP, Payne MC, Kondor R, Csányi G. Gaussian approximation potentials: the accuracy of quantum mechanics, without the electrons. *Phys Rev Lett* 2010;104:136403. DOI PubMed

20. Deng B, Zhong P, Jun K, et al. CHGNet as a pretrained universal neural network potential for charge-informed atomistic modelling. *Nat Mach Intell* 2023;5:1031-41. DOI

21. Takamoto S, Shinagawa C, Motoki D, et al. Towards universal neural network potential for material discovery applicable to arbitrary combination of 45 elements. *Nat Commun* 2022;13:2991. DOI PubMed PMC

22. Chen C, Ong SP. A universal graph deep learning interatomic potential for the periodic table. *Nat Comput Sci* 2022;2:718-28. DOI PubMed

23. Dai FZ, Wen B, Sun Y, Xiang H, Zhou Y. Theoretical prediction on thermal and mechanical properties of high entropy $(Zr_{0.2}Hf_{0.2}Ti_{0.2}Nb_{0.2}Ta_{0.2})C$ by deep learning potential. *J Mater Sci Technol* 2020;43:168-74. DOI

24. Dai FZ, Sun Y, Wen B, Xiang H, Zhou Y. Temperature dependent thermal and elastic properties of high entropy $(Ti_{0.2}Zr_{0.2}Hf_{0.2}Nb_{0.2}Ta_{0.2})B_2$: molecular dynamics simulation by deep learning potential. *J Mater Sci Technol* 2021;72:8-15. DOI

25. Dai FZ, Wen B, Sun Y, Ren Y, Xiang H, Zhou Y. Grain boundary segregation induced strong UHTCs at elevated temperatures: a universal mechanism from conventional UHTCs to high entropy UHTCs. *J Mater Sci Technol* 2022;123:26-33. DOI

26. Dai FZ, Wen B, Xiang H, Zhou Y. Grain boundary strengthening in ZrB_2 by segregation of W: atomistic simulations with deep learning potential. *J Eur Ceram Soc* 2020;40:5029-36. DOI

27. Zhang D, Liu X, Zhang X, et al. DPA-2: towards a universal large atomic model for molecular and material simulation. arXiv. [Preprint.] Dec 24, 2023 [accessed 2024 Aug 8]. Available from: https://arxiv.org/abs/2312.15492.

28. Zhang D, Bi H, Dai FZ, et al. Pretraining of attention-based deep learning potential model for molecular simulation. *npj Comput Mater* 2024;10:94. DOI

29. Zhang L, Lin DY, Wang H, Car R, Weinan E. Active learning of uniformly accurate interatomic potentials for materials simulation. *Phys Rev Mater* 2019;3:023804. DOI

30. Kresse G, Furthmüller J. Efficiency of ab-initio total energy calculations for metals and semiconductors using a plane-wave basis set. *Comput Mater Sci* 1996;6:15-50. DOI

31. Blöchl PE. Projector augmented-wave method. *Phys Rev B Condens Matter* 1994;50:17953-79. DOI PubMed

32. Perdew JP, Burke K, Ernzerhof M. Generalized gradient approximation made simple. *Phys Rev Lett* 1996;77:3865-8. DOI PubMed

33. Pack JD, Monkhorst HJ. "Special points for Brillouin-zone integrations" - a reply. *Phys Rev B* 1977;16:1748-9. DOI

34. Wang H, Zhang L, Han J, Weinan E. DeePMD-kit: a deep learning package for many-body potential energy representation and molecular dynamics. *Comput Phys Commun* 2018;228:178-84. DOI

35. Zeng J, Zhang D, Lu D, et al. DeePMD-kit v2: a software package for deep potential models. *J Chem Phys* 2023;159:054801. DOI

36. Plimpton S. Fast parallel algorithms for short-range molecular dynamics. *J Comput Phys* 1995;117:1-19. DOI

37. Ma HB, Zhang GJ, Liu HL, Liu JX, Lu Y, Xu FF. Effect of WC or ZrC addition on thermal residual stresses in ZrB_2-SiC ceramics. *Mater Design* 2016;110:340-5. DOI

38. Ruby E, Windsch, Chang Y. Ternary phase equilibria in transition metal-boron-carbon-silicon systems. Available from: https://www.

semanticscholar.org/paper/Ternary-phase-equilibria-in-transition-systems-Ruby-Windsch/2d30dae05430ca0696e725f9a05b98aa47a02e88. [Last accessed on 8 Aug 2024].

39. Ma HB, Zou J, Zhu JT, Liu LF, Zhang GJ. Segregation of tungsten atoms at ZrB_2 grain boundaries in strong ZrB_2-SiC-WC ceramics. *Scr Mater* 2018;157:76-80. DOI

40. Su W, Chen L, Zhang W, Huo S, Wang Y, Zhou Y. Insights into grain boundary segregation and solubility limit of Cr in (TiZrNbTaCr)C. *J Mater Sci Technol* 2023;139:1-9. DOI

41. Su W, Chen L, Huo S, Zhang W, Wang Y, Zhou Y. Fracture mode transition from intergranular to transgranular in (TiZrNbTaCr)C: the grain boundary purification effect of Cr carbide. *J Eur Ceram Soc* 2024;44:1881-9. DOI

42. Dai FZ, Zhou Y, Sun W. Segregation of solute atoms (Y, Nb, Ta, Mo and W) in ZrB_2 grain boundaries and their effects on grain boundary strengths: a first-principles investigation. *Acta Mater* 2017;127:312-8. DOI

43. Silvestroni L, Kleebe HJ, Fahrenholtz WG, Watts J. Super-strong materials for temperatures exceeding 2000 °C. *Sci Rep* 2017;7:40730. DOI PubMed PMC

44. Mo P, Li C, Zhao D, et al. Accurate and efficient molecular dynamics based on machine learning and non von Neumann architecture. *npj Comput Mater* 2022;8:107. DOI

45. Jain A, Ong SP, Hautier G, et al. Commentary: the materials project: a materials genome approach to accelerating materials innovation. *APL Mater* 2013;1:011002. DOI

46. Curtarolo S, Setyawan W, Wang S, et al. AFLOWLIB.ORG: a distributed materials properties repository from high-throughput ab initio calculations. *Comput Mater Sci* 2012;58:227-35. DOI

47. Saal JE, Kirklin S, Aykol M, Meredig B, Wolverton C. Materials design and discovery with high-throughput density functional theory: the Open Quantum Materials Database (OQMD). *JOM* 2013;65:1501-9. DOI